DOI: 10.15480/882.9354

Eighth International Symposium on Marine Propulsors
smp'24, Berlin, Germany, March 2024

Numerical Study of Propeller Slipstream Characteristics during Berthing and Unberthing Maneuvers of a RORO Vessel

K. Wang[1], M. Abdel-Maksoud[1], M. Weiss[1] J. Aberle[2]
P. Pinkenburg[3], J. Macías Lezcano[2], A. I. Llull Marroig[2]

[1]TU Hamburg, Hamburg, Germany
[2]TU Braunschweig, Braunschweig, Germany
[3]WK Consultants GmbH, Hamburg, Germany

ABSTRACT

For the investigation of the impact of the propeller slipstream on the port facilities, detailed analyses are carried out using a Reynolds-Averaged Navier-Stokes (RANS) method. The characteristics of the propeller flow field were studied, taking into account operating conditions during berthing and unberthing, interactions with the ship hull, quay wall and harbor bed. To obtain the necessary maneuvering data, information was extracted from the voyage data recorder (VDR) of a twin-screw RORO vessel during berthing and unberthing in the Port of Lübeck-Travemünde. Automatic identification system (AIS) and VDR data sets were collected and analyzed to identify conditions of interest for the numerical investigations. The vessel is equipped with two flap rudders and two bow thrusters. RANS simulations were performed for different rudder angles and number of revolutions of the main propellers (MPs) and transverse thrusters (TTs). The simulation results include unsteady velocity and pressure distributions in the flow field near the quay walls and harbor bed, considering different positions and orientations of the ship relative to the quay walls. The calculated maximum axial induced velocities are compared with those obtained using the semi-empirical formulae. In addition, the proper orthogonal decomposition (POD) on the harbor bed was used to evaluate the wall shear stress (WSS) and turbulent kinetic energy (TKE) to identify locations of maximum scour potential. The numerical results were thoroughly evaluated and analyzed to provide a robust basis for future extensions of the semi-empirical formulae.

Keywords

Propeller Slipstream, Harbor Maneuver, RANS Simulations, Maneuvering Devices, VDR-Data.

1 INTRODUCTION

With the continuous growth in ship dimensions in recent years, the installed power for the propulsion and maneuvering devices must also be increased, which leads to correspondingly high velocities in the slipstream generated by the propellers. Accurate prediction of the velocities induced by the main propellers and the bow thrusters is therefore crucial, as the scour and erosion generated by the propeller slipstream due to the interaction with the quay walls and harbor bed may ultimately threaten their stability and that of nearby structures. Considering the potential consequences, early detection and continuous monitoring of the velocity and pressure distribution in the propeller slipstream play a crucial role in protecting the integrity of port facilities.

When a ship operates in a restricted area, such as during berthing and unberthing maneuvers, the propeller jet is reflected by the quay wall and directed towards the bed, causing erosion of the bed. Understanding the characteristics of the propeller jet is essential to protect the bed structure. The velocity distribution close to the bed depends on many parameters such as propeller characteristics, engine power, rudder arrangement, under-keel clearance and distance between propeller and quay wall. These are the main parameters used in both formulations of the German and Dutch methods (PIANC 2015) for the estimation of the maximum near-bed velocity. These two methods are based on the maximum velocity in the propeller jet.

Existing approaches to determine the maximum velocity in the propeller jet are mostly based on experimental investigations. In the experimental studies (Lam et al. 2012, Hamill et al. 2015, Hamill & Kee 2016, Hong et al. 2020), the measured maximum velocity may be underestimated due to the lack of sufficient measurement points and the uncertain defined efflux plane. In addition, most experiments have been carried out on open propellers, and the investigations on ducted propellers, particularly in the interaction with a ship's hull and rudders, is very limited.

The development of the slipstream also varies under different operating conditions, such as propeller operating in a confined area. Wei & Chiew (2019) conducted an experimental study of propeller slipstreams impinging on vertical quay walls using the PIV technique, and found that the development of the jets was governed by both jet diffusion and wall obstruction mechanisms at different wall clear-

ances. Three flow regions can be identified, i.e., the free jet region, the impingement region and the wall-jet region. In the presence of a plane boundary, Wei et al. (2017) also point out the formation of these three regions and that the propeller slipstream loses its symmetry around the centerline. This phenomenon is known as the Coanda effect. For a confined propeller slipstream, the accurate delineation of the longitudinally defined regions, namely the zone of flow establishment (ZFE) and the zone of established flow (ZEF), remains a critical issue. Semi-empirical formulae designed primarily for free jet expansion may have limited applicability in such scenarios and may need to be revised.

PIANC (2015) explains that the linear superposition of the flow field velocities induced by multiple propellers may result in an increase in the total axial impulse of the superimposed jets. According to the experimental results conducted by Mujal-Colilles et al. (2018), he suggested the use of quadratic superposition in both the German and the Dutch method, especially in situations without a rudder. However, a rudder can split the jet into two distinct flows - one towards the free surface and the other towards the bed (Hamill & McGarvey 1997). The velocity of the slipstream can increase by 30% compared to the jet without presence of the rudder, potentially leading to an increased erosion on the bed.

As all maneuvering devices are activated during berthing and unberthing maneuvers in the restricted harbor area, various flow phenomena such as diffusion flow, impingement flow, deflected flow and swirling flow can interact and lead to high dynamic loads on the harbor bed.

In this study, a numerical approach is presented to demonstrate these phenomena.

2 VESSEL OF INVESTIGATION

In this paper, the unberthing and berthing of a twin-screw RORO vessel is investigated. The ship is owned by the Finnlines Group. The vessel's overall length (LOA) is $217.78\,\mathrm{m}$ and its length between perpendiculars (LPP) is $199.20\,\mathrm{m}$. It has a breadth (B_{MOULDED}) of $26.50\,\mathrm{m}$ and a design draft (T_{DESIGN}) of $6.80\,\mathrm{m}$. The vessel is equipped with two flap rudders and two bow thrusters. Detailed specifications can be found in Table 1. Figure 1 shows a photo of a Finnlines vessel sailing in the port of Lübeck-Travemünde.

Table 1: The main features of the investigated vessel.

L_{OA} [m]	217.78
L_{PP} [m]	199.20
B_{MOULDED} [m]	26.50
T_{DESIGN} [m]	6.80
D_{SP} [m]	5.00
$n_{\mathrm{max\,SP}}$ [rpm]	132.00
D_{TT} [m]	2.00
$n_{\mathrm{max\,TT}}$ [rpm]	307.00
v_{DESIGN} [kn]	20

Figure 1: The MS Finntide in Travemünde.

3 SIMULATIONS OF CONDITIONS OF INTEREST

In order to thoroughly investigate the propeller slipstream-characteristics, it is essential to start with an analysis of the existing data. The next step is to determine the availability and relevance of the data provided, which relate to the berthing and unberthing maneuvers of the Finnlines vessel in the port of Lübeck-Travemünde.

AIS data contains time series information associated with the global positioning system (GPS) position: longitude (LON) and latitude (LAT), speed over ground (SOG), heading (HDG) and course over ground (COG). Figure 2 shows the trajectory of the vessel during arrival and departure as extracted from the AIS data for a selected maneuver. The red empty circles correspond to the bow position at a particular time, while the other two dots indicate the bridge and stern positions respectively.

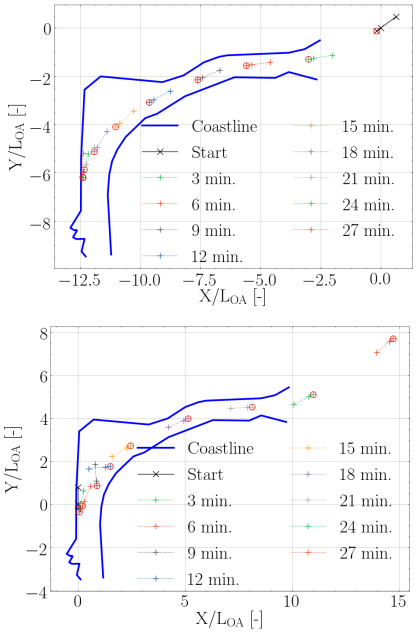

Figure 2: Trajectories of the ship during berthing (top) and unberthing (bottom) maneuvers.

As the AIS data lacks information such as rudder angle,

propeller speed and pitch, the use of the VDR is required. The chosen scenario for the berthing maneuver, as shown in Figure 3, occurs when the vessel is pushing away from the quay using the bow thrusters. In this context, several factors come together to maximize the impact on the bed and the quay wall. On the one hand, the power consumed by the bow thrusters is more than 80% of their engine power. On the other hand, both the water depth under the keel (3.8 m) and the distance to the quay (1 m) are minimal. The chosen time is around 15:47 local time on that day, which coincides with the peak power output from the bow thruster, as shown in Figure 4, where TT2 denotes the TT closer to the bow compared to TT1.

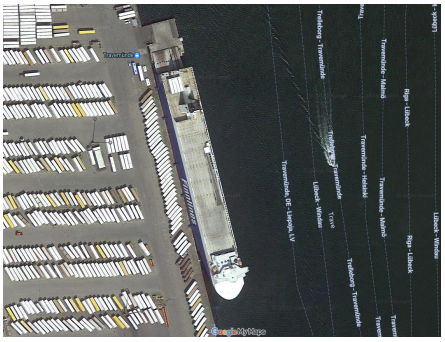

Figure 3: The position of the vessel for numerical studies at berthing and unberthing maneuvers (©Google Maps).

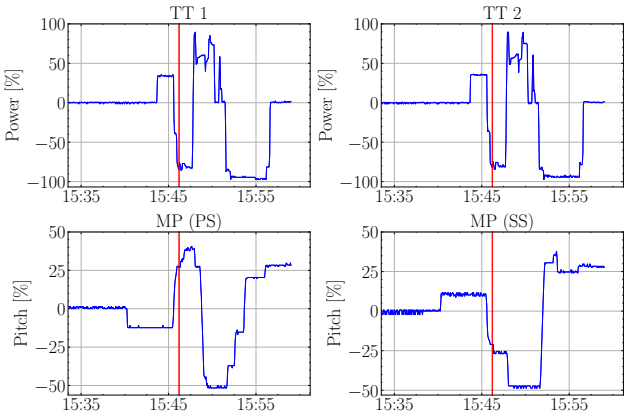

Figure 4: VDR departure data with the situation marked for the numerical simulation: June 22, 2023, at 15:47 local time.

The scenario chosen for the berthing maneuver was to use the bow thrusters to gently guide the ship against the wall until it was securely moored. In contrast to the unberthing maneuver, the force applied by the bow thrusters during the berthing maneuver is significantly lower. Both bow thrusters produce a jet that counteracts the direction of the force applied during berthing, potentially mitigating the erosive effects.

When the port side (PS) propeller is operating at positive pitch and zero deflected rudder angle, it generates a direct impingement flow on the quay wall. To provide a comprehensive representation, the average of the monitoring response was calculated, taking into account the extended duration between 7:11 and 7:12 (see Figure 5). Despite this, the ship's position remains consistent with that observed during the unberthing maneuver, as shown in Figure 3.

The operating conditions for the propeller and rudder in both scenarios are summarized in Table 2.

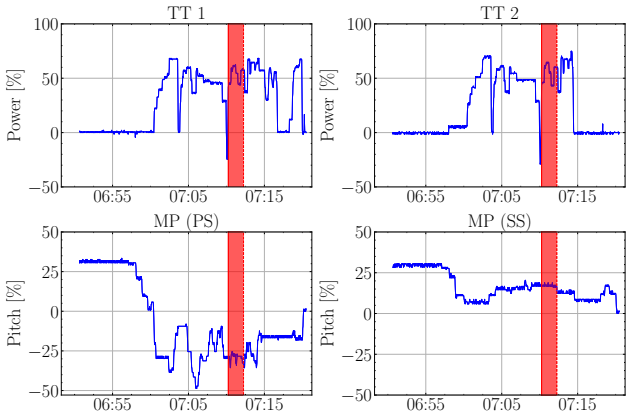

Figure 5: VDR arrival data with the situation marked for the numerical simulation: June 15, 2023, approximately 7:11 AM local time.

Table 2: Selected operating conditions from VDR for numerical simulations.

	Unberthing	**Berthing**
n_{TT} [Hz]	290/60	250/60
n_{MP} [Hz]	132/60	132/60
Pitch PS [%]	30	-30
Pitch SS [%]	-20	20
Rudder PS [°]	25	0
Rudder SS [°]	0	0

4 NUMERICAL SIMULATIONS

The commercially available RANSE solver STAR-CCM+ Version 2206 Build 17.04.008 is applied for the numerical calculations. The finite volume method (FVM) is used to calculate the flow around the ship. In FVM, the computational domain is discretized by a finite number of control volumes. For each control volume, conservation equations are defined for the individual flow variables. In the present study, the $k-\omega$ SST turbulence model (Menter et al. 2003) is used to obtain a closed system of equations. The second-order upwind scheme is applied for the less numerical diffusion compared to the first-order scheme. For the selection of the temporal discretization the second-order is used and the time step is set to

$$\mathrm{ts} = 1/(360 \cdot \mathrm{n_{TT}}).$$

The rotation rate of the bow thruster (n_{TT}) ensures that the impeller rotates 1 degree per time step. Owing to the distinct revolutions between the main propellers and tunnel propellers, the main propellers rotate by less than 1 degree per time step.

The computational domain is divided into two distinct regions: the stationary region and the rotating region. The

stationary region includes the rudder and hull meshes, while the rotating region includes the four propeller meshes - two for the main twin propellers and two for the tunnel thruster propellers. These stationary and rotating regions are connected by sliding interfaces. To ensure smooth flow variables across the interface, it is essential that the mesh resolutions on both sides are comparable.

The solver uses the over-set mesh technique to reasonably adapt the mesh to different rudder angles, including the flap angle under different operating conditions. The over-set mesh is implemented between the movable flap, the main rudder blade and the background mesh. The simulation duration for a single run (one situation) extends to approximately one week, utilizing 160 processors offered by the HPC cluster at TUHH. The total number of cells involved in the simulation amounts to around 83 million. The overall representation of the mesh is shown in Figure 6.

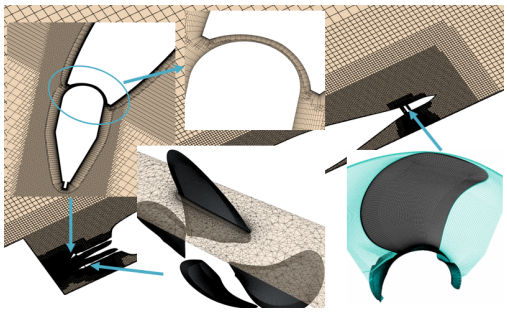

Figure 6: Computational mesh.

As mentioned above, the propellers operate within a confined area, with an assumed under-keel clearance of $3.8\,\mathrm{m}$ and the narrowest distance being $1\,\mathrm{m}$ between the ship and the quay wall. At the stern, two ramps are available for fast loading and unloading onto the platform.

The simulated flow characteristics do not take into account changes in water level, tidal currents, wind and waves. Additionally, the deformation of the free surface is disregarded and treated as a slip wall. At the selected moment for both simulations, the ship's velocity is nearly zero, resulting in consistent boundary conditions at the inlet and outlet where the pressure equals atmospheric pressure. The numerical domain's dimensions are illustrated in Figure 7.

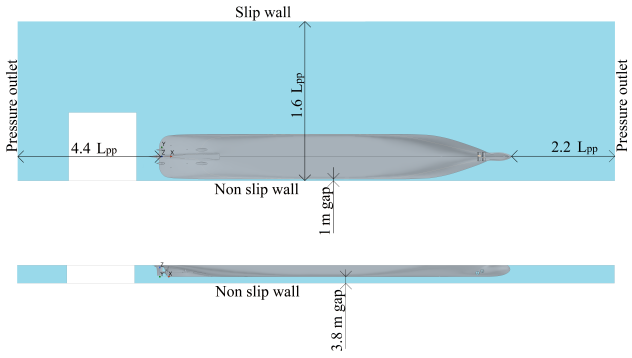

Figure 7: Boundary conditions: top and side views.

5 NUMERICAL RESULTS

Typically, the simulation can be performed at any time during the berthing and unberthing maneuvers based on the VDR data. However, in a critical scenario, it is advisable to prioritize the consideration of the effects of TTs and MPs. This study focuses primarily on two situations: departure and arrival, as mentioned previously. For departure, the study investigates the impact of TTs, while for arrivals, the focus is on the influence of MPs on harbor bed flow patterns. The specific flow characteristics of the analyzed cases are shown individually.

5.1 Effects of Bow Thrusters at Unberthing

In the first case, the primary investigations focus on the impact of the slipstream generated by the bow thrusters on the surrounding environment. These effects are explained through the analysis of variables such as velocity and pressure distributions. Specific planes downstream of the propeller are employed to capture the velocity evolution induced by both TTs.

Output parameters including pressure, WSS, and TKE are locally stored for subsequent evaluation. Besides, several observation points are pre-defined to represent the pressure impulse. The longitudinal location of these points is chosen between the two bow thrusters. The spacing between neighboring points along the quay wall and the bed are 1.06·R and 2·R correspondingly, as illustrated in Figure 8, where R is the radius of the tunnel propeller.

The dataset is derived based on the last 10 revolutions of the tunnel propellers, with a data output frequency five times higher than that of the propellers.

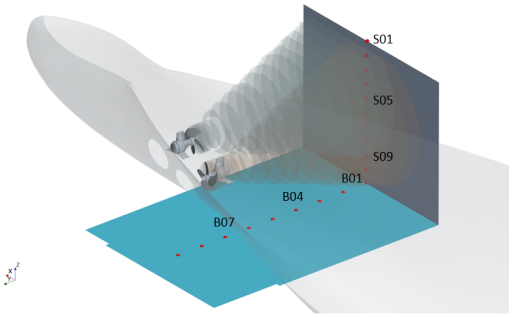

Figure 8: Definition of the locations for collecting flow data in the bow area.

5.1.1 Efflux Velocity

The propeller is operating in a tunnel where the mean flow rate should remain constant over the same cross-section area. The local flow characteristics, such as the tip vortex of the propeller, can have a significant effect on finding the maximum velocity. Therefore, the mean velocity is calculated by averaging the velocities over the circumference to reduce the influence of the localized flow. The plane is radially divided into 100 segments and the velocities on each segment can be averaged. From the averaged velocity profile over the radius, the maximum velocity and its radial position for TT1 and TT2 are determined, see Ta-

ble 3 and Table 4, respectively. In tunnel 1, the axial flow velocity downstream of the propeller exhibits more significant variations, mainly attributed to the configuration of the housing. The pulling configuration induces a blockage effect, resulting in excessive flow velocity that is higher than $10\,\mathrm{m\,s^{-1}}$.

In general, the variation of the maximum axial velocity does not change too much inside the tunnel. The tunnel exit is located approximately $1{\cdot}D_{TT}$ from the propeller plane of TT1 and $0.75{\cdot}D_{TT}$ from the propeller plane of TT2. The corresponding stations can be assumed to be an efflux plane where the effect of flow diffusion is not yet pronounced. The corresponding maximum velocities, $9.51\,\mathrm{m\,s^{-1}}$ and $9.50\,\mathrm{m\,s^{-1}}$, are considered as efflux velocities.

Table 3: Maximum circumferentially averaged axial velocity for TT1.

y/D	Max circ. vel [$\mathrm{m\,s^{-1}}$]	r/R
0.25	9.51	0.89
0.13	9.11	0.87
0.50	10.32	0.91
0.75	9.65	0.88
1.00	9.51	0.90
1.25	9.11	0.88

Table 4: Maximum circumferentially averaged axial velocity for TT2.

y/D	Max circ. vel [$\mathrm{m\,s^{-1}}$]	r/R
0.13	9.76	0.90
0.25	9.67	0.90
0.35	9.57	0.90
0.50	9.55	0.90
0.75	9.50	0.90
1.00	8.20	0.86

Núñez-González et al. (2018) arranged the efflux velocity formula as shown in Equation (1), where D_p is the diameter of the propeller, D_0 is the diameter of the contracted slipstream and n_p is the propeller rotation rate; for non-ducted propellers, the relationship between the two diameters is $D_p/D_0 = \sqrt{2}$, while for ducted propellers, if there is no jet contraction, both diameters are the same. K_t is the thrust coefficient of the propeller. If the installed engine power P_d is known, the efflux can be estimated using Equation (2) derived from Blaauw & Van de Kaa (1978). Both K_t and P_d can be obtained from the numerical simulations.

$$u_0 = \frac{2}{\sqrt{\pi}} n_p D_p \sqrt{K_t} \frac{D_p}{D_0} \tag{1}$$

$$u_0 = \alpha \left(\frac{P_d}{\rho {D_p}^2} \right)^{1/3} \begin{cases} \alpha = 1.17 & \text{for ducted propeller} \\ \alpha = 1.48 & \text{for non-ducted propeller} \end{cases} \tag{2}$$

The values determined by CFD computations are higher than the velocity derived from the semi-empirical formulation, as shown in Table 5. One of the factors contributing to this discrepancy is attributed to the blockage effect induced by the housing as mentioned before. Another reason could be associated with the formula itself. Most of the formulas are derived from the momentum theory, assuming a homogeneous velocity distribution independent of the actual operation condition.

Table 5: Comparison of efflux velocity between CFD and semi-empirical results for unberthing.

	CFD		Equation (1)		Equation (2)	
	TT1	TT2	TT1	TT2	TT1	TT2
u_0 [$\mathrm{m\,s^{-1}}$]	9.51	9.50	5.69	5.44	7.56	7.19

Influence of the mesh size on the efflux velocity

To assess the effect of mesh resolution on the efflux velocity, a mesh study was performed. To reduce computational time, this study was limited to the foreship area, extending only up to the midship section. In addition, only TT2 was included in the simulation. Instead of globally increasing the number of cells, local mesh refinement was applied, especially downstream of the tunnel propeller. Figure 9 illustrates the three mesh resolutions used in this study, where an azimuth angle of 90° indicates the stern direction.

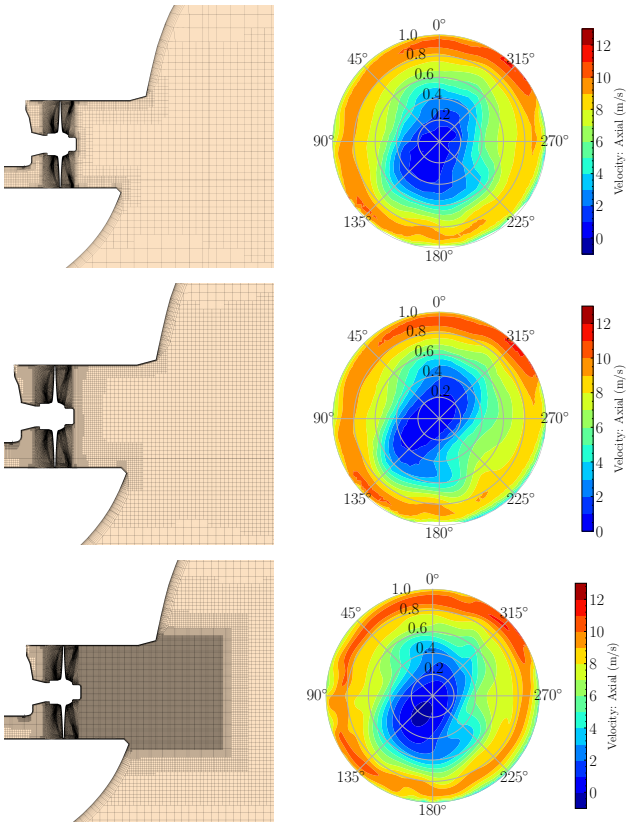

Figure 9: Average axial velocity distribution, seen from the quay wall, obtained from 40 tunnel propeller revolutions on the tunnel exit plane (y/D=0.75 in Table 4) with respect to the three mesh resolutions. From top to bottom: coarse mesh, medium mesh and fine mesh.

The calculated efflux velocities using the averaged axial flow field over 40 revolutions, as shown in Figure 9, are presented in Table 6. As the resolution increases, the efflux velocity decreases, with a 3.8% difference between course and fine meshes, and an even smaller, almost negligible difference between medium and fine meshes. Therefore, the resolution of "Mesh 2" was adopted for its balance of accuracy and efficiency.

Table 6: Efflux velocity for different meshes.

	Cells [million]	u_0 [$\mathrm{m\,s^{-1}}$]
Mesh 1	13.6	9.83
Mesh 2	16.1	9.50
Mesh 3	30.3	9.47

5.1.2 Induced Velocity at Harbor Bed

In the experiments conducted by Schmidt (2000), the propeller slipstream was divided into five parts, as shown in Figure 10. The conversion between velocity and pressure is a critical aspect of the interaction process. When the slipstream hits the quay wall,it will be then directed vertically towards the harbor bed where the kinetic energy (velocity) is converted to pressure. Once the slipstream reaches the bed, the potential energy is converted back into kinetic energy. The maximum velocity in region V is a valuable reference point for assessing the erosion stability of the bed. Two approaches are used to obtain this velocity. The first approach is to locally define a volumetric region near the junction of the bed and the quay wall. Since the bottom is a non-slip boundary condition, a special volume with dimensions $4.75D_{TT}\times5D_{TT}\times0.2D_{TT}$ (L×B×H) must be set up to capture the maximum velocity directly. An alternative is the indirect method, as introduced by Abramowicz-Gerigk et al. (2018) and Abramowicz-Gerigk & Jachowski (2022), which uses the Bernoulli equation to calculate the near-bed velocity from dynamic pressure measurements at the quay wall, as pressure sensors could not be installed on the harbor bed due to potential damage risks.

For a 2D case, the change in pressure at the quay wall might be representative of the change in bed velocity. But with a 3D flow, after hitting the wall, the flow will disperse in all directions, and there is bound to be a loss of potential energy, resulting in an increase in the predicted bed velocity in the 2D case. For this reason, in CFD calculations, the maximum pressure was not only determined on the quay wall but also on the harbor bed. Figure 11 clearly shows that the difference in the mean velocity between the two approaches is very close. However, the deviation of the velocity fluctuation calculated by the maximum dynamic pressure is around 25% relative to its mean velocity. The flow field may not be steady.

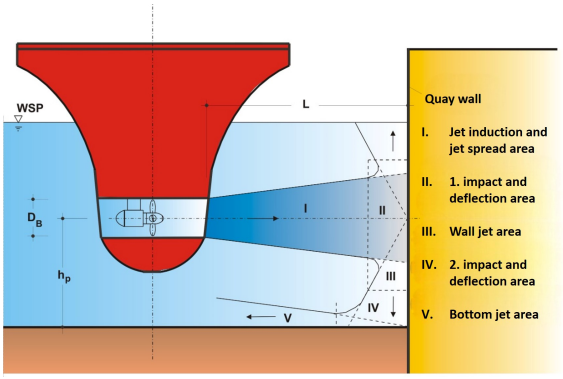

Figure 10: Division of the jet flow field into five zones classified by Schmidt (2000).

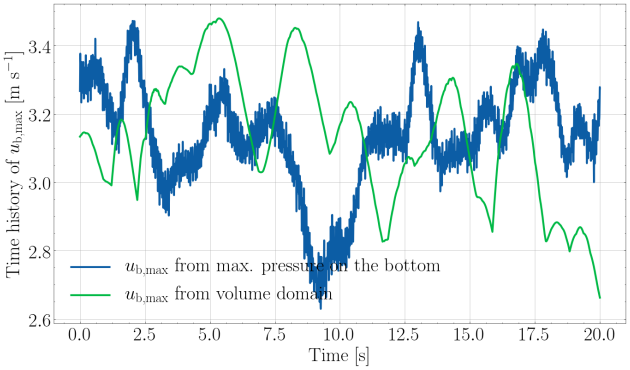

Figure 11: Maximum velocity at the harbor bed. The average of the two curves within the 20 s is $3.136\,\mathrm{m\,s^{-1}}$ and $3.140\,\mathrm{m\,s^{-1}}$, respectively.

PIANC (2015) suggests that the maximum velocity at the harbor bed can be calculated by the German and the Dutch method in terms of Equation (3) and Equation (4), respectively, where L is the distance between tunnel exit and quay wall and h is the vertical distance between propeller rotation axis and harbor bed. α_L is a factor dependent on both parameter L and h, which are different according to the different position of TT1 and TT2.

However, the formulae do not take into account the effect of multiple jets. The total velocity may be quadratically superimposed (PIANC 2015). The resultant velocity and the geometrical parameters used are shown in Table 7. Note that the efflux velocity u_0 used in Equation (3) and Equation (4) is derived from Equation (2), which provides the maximum efflux velocity within the semi-empirical formulas, as shown in Table 5.

The German method indicates a difference in the maximum bed velocity estimation, whereas the agreement between CFD with $3.14\,\mathrm{m\,s^{-1}}$ and the Dutch method with $3.01\,\mathrm{m\,s^{-1}}$ is very close. CFD provides only a 4% increase in the maximum bed velocity compared to the Dutch method.

$$u_{\mathrm{b,max}}(\mathrm{German}) = u_0\alpha_L 1.9\left(\frac{L}{D_p}\right)^{-1} \qquad (3)$$

$$u_{\mathrm{b,max}}(\mathrm{Dutch}) = \begin{cases} u_0 \left(\frac{D_p}{h}\right) & \text{for L/h} < 1.8 \\ 2.8u_0 \left(\frac{D_p}{L+h}\right) & \text{for L/h} \geq 1.8 \end{cases} \quad (4)$$

Table 7: Calculation of the maximum bed velocity caused by individual jet using the semi-empirical formulas.

	TT1	TT2	Resultant Vel.
L/h	2.13	1.72	
L/D_p	6.39	6.17	
h/D_p	3.00	3.58	
α_L	0.45	0.40	
$u_{\mathrm{b,max}}$ [$\mathrm{m\,s^{-1}}$] German	1.01	0.89	1.35
$u_{\mathrm{b,max}}$ [$\mathrm{m\,s^{-1}}$] Dutch	2.26	2.01	3.02

5.1.3 Pressure Fluctuation

The change in pressure at various predefined locations (see Figure 8) may capture some flow characteristics. As shown in Figure 12, at B01, the heel of the quay wall, the frequency of the prominent fluctuation is significantly lower than the frequency of the blades whereas at B07, the frequency of the blades is quite noticeable. At B04, both dominant pressure amplitudes are comparable. However the amplitude of the first-order blade frequency exhibits a minor variation across the three points.

Considering the flow after it hits the bed (part V in Figure 10), the flow there can be entrained by the jet in part I. This process results in a very strong reflux between I and V. This is likely to be the largest source of low-frequency contribution, producing a maximum pressure amplitude that is more than four times the amplitude from the first order blade frequency at the corner point B01. A process in terms of intermittency and entrainment between part I and part V can be the main cause of the spread of turbulent flow, leading to an unsteady flow field in a confined area, as depicted by the limiting streamlines shown in Figure 13.

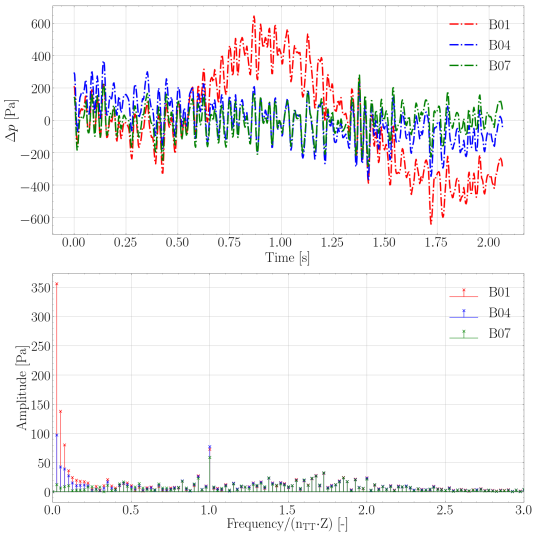

Figure 12: Pressure fluctuation and corresponding FFT analyze on the bed observation points, as indicated in Figure 8

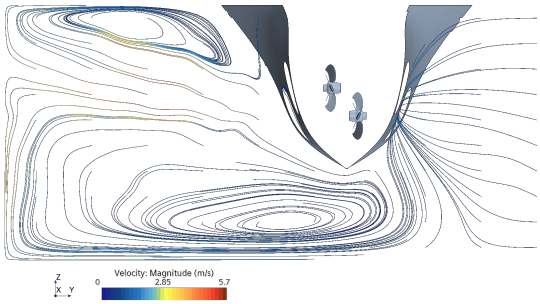

Figure 13: Limiting streamlines on a cross-section located between the thrusters.

5.2 Effects of Main Propellers at Berthing

In case of the berthing maneuver, the propeller on the starboard side has a positive pitch, while the propeller on the PS operates at a negative pitch.

The efflux velocity data is based on the last 10 revolutions of the tunnel thrusters, corresponding to 4.55 revolutions of the main propellers. For the POD analysis, the time period is about 9 s. The number of snapshots is 3176.

Both the propellers in combination with zero-angle flap rudders are shown in Figure 14.

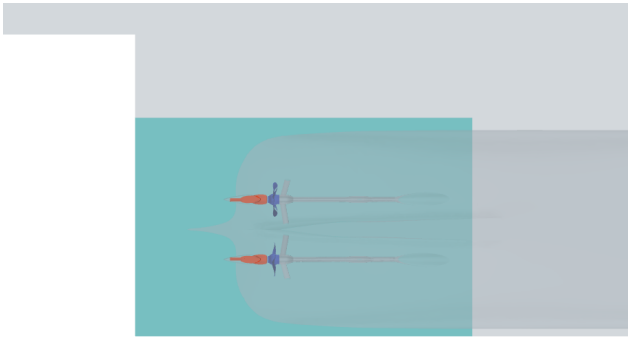

Figure 14: Definition of the location (blue area) for collecting flow data on the bed (the stern area in Figure 7).

5.2.1 Efflux Velocity

The efflux velocity is calculated from the SS propeller. The procedure for determining the velocities is similar to that described for the transverse thrusters. If a rudder is present, it may not be possible to determine the location of the efflux plane, especially the contracted portion of the slipstream. Therefore, the efflux velocity is determined from the plane of maximum circumferential average axial velocity between the propeller plane and the leading edge of the rudder. In addition, the propeller is not operating at its design pitch, so there may be a reduction in propeller performance. As a result, the simulated velocity value is observed to be lower than the predicted value derived from Equation (2). Table 8 summarized the calculated efflux velocities in

terms of the numerical simulation and the semi-empirical formulae.

Table 8: Comparison of efflux velocity between CFD and semi-empirical results for berthing.

	MP (SS)		
	CFD	Equation (1)	Equation (2)
u_0 [m s^{-1}]	5.57	5.13	6.3

5.2.2 Bed Loads

Kim et al. (2000) emphasize that both shear stress on the bottom and the structure of near-bed turbulence play a key role in influencing sediment transport. In addition, a study by Ferraro et al. (2022) highlighted the effect of flow intensity on scour hole evolution. The current simulation does not account for bed deformation, but by showing the WSS and TKE on the flat bed, it can generally represent the onset of the scour process. The simulated WSS and TKE on the selected part of bed are shown in Figure 15 and Figure 16, respectively. The distributions of both WSS and TKE exhibit a very strong correlation.

In both figures, POD was applied to extract the essential features of the flow field using the first four modes, which account for more than 80% of the total energy (Table 9). The reconstruction of the flow field is achieved by combining the time-averaged flow field with fluctuations derived from the first four modes. The red area on the lower left corresponds to WSS or TKE caused by the reflected flow after hitting the quay wall and bed. On the right hand side, the red area is due to the flow passing through the narrow clearance between the skeg and the bed. This phenomenon may be explained by the fact that the induced velocities of the two propellers are in different directions, leading to the inherent circulating flow under the skeg. Meanwhile, the skeg can direct the circulating flow toward the bed.

The interpretation of the POD modes can be linked to the explanation provided by Weiss (2019). According to Weiss, regions of the same color in the POD modes tend to show correlated fluctuations, while regions of different colors indicate anti-correlation between the fluctuations. As can be seen from the modes shown in the figures, the reflected flow exhibits a wave-like pattern. The blue and red regions alternate progressively and spread along the walls. However, detecting this flow feature in both instantaneous as well as mean flow fields can be very challenging.

Table 9: Energy distribution of the first four selected modes according to TKE.

	Mode 1	Mode 2	Mode 3	Mode 4
Energy [%]	42.8	18.5	14.3	5.5

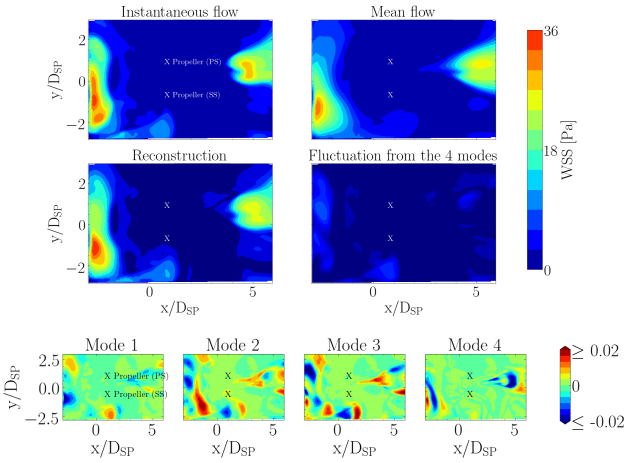

Figure 15: WSS on the bed (blue area in Figure 14) at an instantaneous flow field and the reconstructed WSS using the first 4 modes of WSS fluctuations.

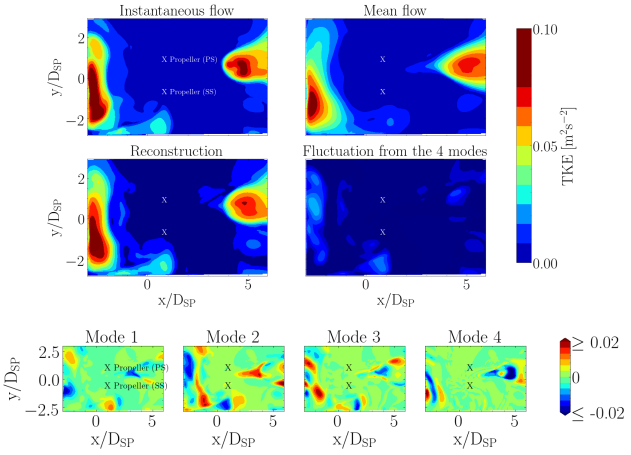

Figure 16: TKE on the bed (blue area in Figure 14) at an instantaneous flow field and the reconstructed TKE field using the first 4 modes of TKE fluctuations.

6 CONCLUSION

The maximum bed velocity induced by the transverse thrusters predicted by CFD and the Dutch approach are in good agreement, while the German approach may underestimate this velocity. It should be noted that the semi-empirical formula does not strictly define how to deal with the merging of two jets. A simple linear superposition may be a conservative choice would lead to an over-protection of the structure of the bed. In terms of the efflux velocity induced by the TTs, the CFD estimation is about 25% higher than the semi-empirical formula. The most likely reason for this is that the empirical formula was developed based on momentum theory and does not take into account the varying blade loads as well as the interaction with the housing.

The erosion of the bed is affected by the pressure of the jet vertically, but also by the WSS in the horizontal direction.

By applying the POD method, it is possible to extract the main features of the flow and identify the correlation of the featured flows, which makes it suitable to classify multiple interactions.

Observation from WSS (Figure 15) and TKE (Figure 16) shows that the highest erosion potential occurs near the toe of the harbor walls. The location of the maximum load and the direction of flow propagation are influenced by the operation conditions of the stern propellers. Table 2 shows that the pitch of the propeller is completely reversed during berthing and unberthing maneuvers. This change can result in significant changes in the position of the maximum load on the bed. In addition, the trajectory of the ship changes during such maneuvers. In view of these considerations, it is highly advisable to reinforce the bed structure, particularly near the toe of the harbor walls. Such reinforcement is essential to prevent harbor bed erosion and to maintain structural stability.

ACKNOWLEDGMENT

The work presented here has been conducted within the project "Propellerstrahl - Propellerstrahlinduzierte Erosionserscheinungen" funded by the funding program for Innovative Technologies in ports (IHATEC II) of the Federal Ministry for Digital and Transport (BMDV). The consortium members are WK Consultants GmbH, Leichtweiß-Institute for Hydraulic Engineering and Water Resources (LWI), TU Braunschweig and Institute for Fluid Dynamics and Ship Theory, TU Hamburg (TUHH).

The authors are grateful for the valuable support provided by Finnlines Ship Management for the project. In addition, the active contribution of the Lübeck Port Authority greatly facilitated the progress of the field measurements.

REFERENCES

Abramowicz-Gerigk, T. and Jachowski, J. (2022). 'Ship Berthing and Unberthing Monitoring System in the Ferry Terminal', Sensors **22**(23), pp. 9133.

Abramowicz-Gerigk, T., Burciu, Z., Górski, W. & Reichel, M. (2018). 'Full scale measurements of pressure field induced on the quay wall by bow thrusters – indirect method for seabed velocities monitoring', Ocean Engineering **162**, pp. 150–160.

Blaauw, H.G. & Van de Kaa, E.J. (1978). 'Erosion of Bottom and Sloping Banks Caused by the Screw Race of Manoeuvring Ships', Delft Hydraulics Lab, Netherlands **202**, pp. 1–12.

Ferraro, D., Lauria, A., Penna, N., & Gaudio, R. (2022). 'Unconfined propeller scour in waterways: The role of flow intensity', Physics of Fluids **34**(9), pp. 095137.

Hamill, G., Kee, C. & Ryan, D. (2015). 'Three-dimension efflux velocity characteristics of marine propeller jets'. Proceedings of the Institution of Civil Engineers - Maritime Engineering **168**(2), pp. 62–75.

Hamill, G.A. & Kee, C. (2016). 'Predicting axial velocity profiles within a diffusing marine propeller jet'. Ocean Engineering. **124**, pp. 104–112.

Hamill, G.A. and McGarvey, J.A. (1997). 'Designing for Propeller Action in Harbours', Coastal Engineering 1996 **58**(10), pp. 4451–4463. American Society of Civil Engineers.

Hong, J.-H., Yeh, P.-H., & Chiew, Y.-M. (2020). 'Prediction of Mean Axial Velocity of a Free Turbulent Propeller Jet', Journal of Hydraulic Engineering **146**(3).

Kim, S.-C., Friedrichs C. T., Maa, J. P.-Y. & Wright, L. D. (2020). 'Estimating Bottom Stress in Tidal Boundary Layer from Acoustic Doppler Velocimeter Data', Journal of Hydraulic Engineering **126**(6), pp. 399-406.

Lam, W. H., Robinson, D. J., Hamill, G. A., Zhao, J. F. & Jia, M. (2012). 'Time-Averaged Velocity and Turbulence Intensity at the Initial Downstream Flow from a Six-Bladed Ship Propeller'. Ocean Engineering. **51**, pp. 85–93.

Menter, F.R. & Kuntz, Martin & Langtry, Robin (2003). 'Ten Years of Industrial Experience with the SST Turbulence Model', Fourth International Symposium on Turbulence, Heat and Mass Transfer, pp. 625–632.

Mujal-Colilles, A., Castells, M., Llull, T., Gironella, X. & Martínez De Osés, X. (2018). 'Stern Twin-Propeller Effects on Harbor Infrastructures. Experimental Analysis', Water **10**(11), pp. 1571.

Núñez-González, F., Koll, K. & Spitzer, D. (2018). 'Experimental study of the velocity field induced by a propeller jet in an inland-ship model and the related bed scour', E3S Web of Conferences **40**, pp. 03029.

PIANC (2015). 'Guidelines for protecting berthing structures from scour caused by ships' PIANC REPORT N° 180. World Association for Waterborne Transportation Infrastructure.

Schmidt, E. (2000). 'Belastungen durch Bugstrahlruder', Dresdner Wasserbauliche Mitteilungen 18, pp. 145–157.

Wei, M-X., Chiew, Y-M & Hsieh, S.-C. (2017). 'Plane boundary effects on characteristics of propeller jets', Experiments in Fluids **58**(10), pp. 141.

Wei, M.-X. and Chiew, Y.-M. (2019). 'Impingement of propeller jet on a vertical quay wall', Ocean Engineering **183**, pp. 73–86.

Weiss, J. (2019). 'A Tutorial on the Proper Orthogonal Decomposition', AIAA Aviation 2019 Forum.